JACS
JOURNAL OF THE AMERICAN CHEMICAL SOCIETY

Article

pubs.acs.org/JACS

Locked *ortho*- and *para*-Core Chromophores of Green Fluorescent Protein; Dramatic Emission Enhancement via Structural Constraint

Yen-Hao Hsu,[†,¶] Yi-An Chen,[†,¶] Huan-Wei Tseng,[†] Zhiyun Zhang,[†] Jiun-Yi Shen,[†] Wei-Ti Chuang,[†] Tzu-Chieh Lin,[†] Chun-Shu Lee,[‡] Wen-Yi Hung,*[,‡] Bor-Cherng Hong,[§] Shih-Hung Liu,[†] and Pi-Tai Chou*[,†]

[†]Department of Chemistry and Center for Emerging Material and Advanced Devices, National Taiwan University, Taipei 10617, Taiwan, R.O.C.

[‡]Institute of Optoelectronic Sciences, National Taiwan Ocean University, Keelung 202, Taiwan, R.O.C.

[§]Department of Chemistry and Biochemistry, National Chung Cheng University, Chia-Yi 62102, Taiwan, R.O.C.

Supporting Information

ABSTRACT: We report the design strategy and synthesis of a structurally locked GFP core chromophore ***p*-LHBDI**, its *ortho*-derivative, ***o*-LHBDI**, and **H2BDI** possessing both *para*- and *ortho*-hydroxyl groups such that the inherent rotational motion of the titled compounds has been partially restricted. ***o*-LHBDI** possesses a doubly locked configuration, i.e., the seven-membered ring hydrogen bond and five-membered ring C(4-5-10-13-14) cyclization, from which the excited-state intramolecular proton transfer takes place, rendering a record high tautomer emission yield (0.18 in toluene) and the generation of amplified spontaneous emission. Compared with their unlocked counterparts, a substantial increase in the emission yield is also observed for ***p*-LHBDI** and **H2BDI** in anionic forms in water, and accordingly the structure versus luminescence relationship is fully discussed based on their chemistry and spectroscopy aspect. In solid, ***o*-LHBDI** exhibits an H-aggregate-like molecular packing, offers narrow-bandwidth emission, and has been successfully applied to fabricate a yellow organic light emitting diodes (λ_{max} = 568 nm, η_{ext} = 1.9%) with an emission full width at half-maximum as narrow as 70 nm.

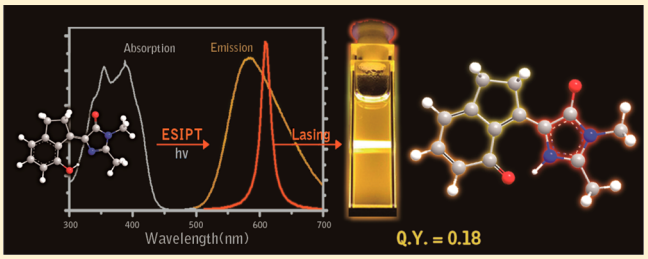

1. INTRODUCTION

Green fluorescent protein (GFP) has been ubiquitously applied in molecular biology and biochemistry.[1−11] The high fluorescence quantum yield of the GFP core chromophore can be attributed to the protein cavity conformation, which can suppress non-radiative relaxation, and to the hydrogen-bond network, which facilitates excited-state proton transfer via a proton relay of water molecules.[12−14] Interestingly, either isolated or synthesized GFP core chromophore (*Z*)-5-(4-hydroxybenzylidene)-2,3-dimethyl-3,5-dihydro-4*H*-imidazol-4-one (***p*-HBDI**, Chart 1, the italic prefix *p* indicates −OH in *para* position with respect to the imidazol-4-one) is non-emissive in its neutral or anion form in solution.[10,15,16] It has been widely accepted that the lack of emission is mainly due to the conformational isomerization via rotation of C(3)−C(4)−C(5) bonds (for numbering, see Chart 1), which acts as the major non-radiative deactivation pathway. Recently, via synthetically switching the hydroxyl group from *para*- to the *ortho*-position of ***p*-HBDI**, the resulting ***o*-HBDI** (Chart 1)[15−17] has an intramolecular hydrogen bond between −OH and N(2) nitrogen, from which ultrafast excited-state intramolecular proton transfer (ESIPT)[18] takes place from hydroxyl proton to N(2) nitrogen, adiabatically forming a proton transfer tautomer in the excited state. The seven-membered ring hydrogen bond in part locks the molecular framework such that the tautomer emission is resolvable at 605 nm with a quantum yield of ∼0.0031 in cyclohexane.[15,16]

Chart 1. Molecular structures for *p*-HBDI, *o*-HBDI, H2BDI, *p*-LHBDI, *o*-LHBDI, and H2LHBDI

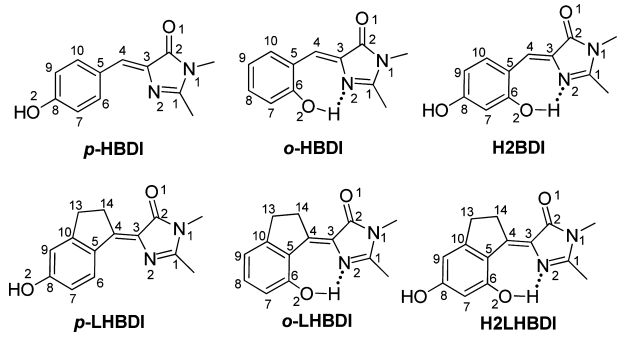

Knowing that structural rigidity plays a pivotal role in emission quantum yields, which are important for future lighting applications, we ponder the possibility of further

Received: June 23, 2014
Published: July 30, 2014

   dx.doi.org/10.1021/ja5062856 | *J. Am. Chem. Soc.* 2014, 136, 11805−11812

locking the C(4)−C(5) rotation of both ***o*-HBDI** and ***p*-HBDI**. Our goals are to provide direct proof of the concept and to dramatically enhance the emission quantum yield, especially in solution, for potential applications. From the synthetic viewpoint, we are seeking to prohibit C(4)−C(5) twisting, feasibly by the cyclization of C(4)−C(5)−C(10), to form locked conformers such as ***o*-LHBDI** and ***p*-LHBDI**, shown in Chart 1. The locked conformation of the GFP core chromophore has previously been achieved by applying a coordination interaction either using a Zn^{2+} ion[19] or a boron (as in a $-BF_2$ group) to enhance fluorescence.[20,21] Moreover, Yang has recently reported an intramolecular N−H−N hydrogen bond that enhances fluorescence.[22] However, to our knowledge, no attempts to synthesize the C4−C5 locked derivatives of GFP chromophore without perturbing the core moiety have been reported. This makes us curious about the synthesis challenge and the associated chemical and photophysical properties.

It turns out that the relevant synthesis is non-trivial, and amid this approach a number of synthetic methodologies have been attempted, especially regarding the locked form of ***p*-HBDI** (vide infra). As a result, ***o*-LHBDI** and ***p*-LHBDI** have been successfully synthesized and show vastly improved emission quantum yields. Even though ***p*-HBDI** is non-emissive, the emission is clearly resolved for ***p*-LHBDI** in both neutral and anion forms. As for ***o*-LHBDI**, the doubly locked configuration, i.e., the seven-membered ring hydrogen bond and five-membered ring C(4−5−10−13−14) cyclization, ensures the structural planarity and rigidity, rendering a record high tautomer emission quantum yield among molecules bearing core benzylidene-imidazolinone moieties. This leads even to the generation of amplified spontaneous emission. The H-type aggregation for ***o*-LHBDI** in solid film leads to a tautomer emission bandwidth of as narrow as ∼70 nm, which is unexpectedly narrow for organic molecules. The narrow emission bandwidth is an advantage in the fabrication of organic light emitting diodes (OLED). Details of the synthetic routes, photochemical properties, and lighting applications are elaborated below.

2. RESULTS AND DISCUSSION

2.1. Syntheses and Structural Characterization. In this work, 7-hydroxy-1-indanone (**7-HI**) and imidazolinone derivatives were used as the starting reactants. These underwent the Knoevenagel condensation reaction[19,20] to produce ***o*-LHBDI** with a good yield (∼63%; see Scheme 1 and Supporting Information (SI) for details). In an unsuccessful approach, we used 5-hydroxy-1-indanone (**5-HI**) as the starting material and applied a similar synthetic protocol in an attempt to synthesize ***p*-LHBDI**, but to no avail. To examine if the solution polarity interfered with the synthesis of ***p*-LHBDI**, the toluene solvent was replaced with others, such as xylene, MeCN, THF, DMSO and DMF. Unfortunately, none brought success, even over a wide range of temperatures. Since a partial positive charge at the carbonyl carbon should increase the neucleophilicity and hence facilitate the condensation reaction, two or more stoichiometric equivalents of Lewis acid, $ZnCl_2$ or $AlCl_3$, were added so that both hydroxyl and carbonyl groups, in theory, would be coordinated. Unfortunately, the attempts to induce reactions were in vain. Table S1 in the SI summarizes all 16 attempts for reference.

A further controlled experiment indicated that Knoevenagel condensation works for 5-methoxyindanone and imidazolinone. Therefore, the hydroxyl proton in **5-HI** seems to be the major retarding group. In order to circumvent the problem, **5-HI** was reacted with Ac_2O in CH_2Cl_2 to form an ester derivative to protect the hydroxyl proton, followed by condensation with imidazolinone using $TiCl_4$ as the Lewis acid in THF[23−25] to obtain (*Z*)-2,3-dihydro-1-(1,2-dimethyl-5-oxo-1*H*-imidazol-4(5*H*)-ylidene)-1*H*-inden-5-yl acetate (***p*-LAcBDI**). Deprotection of ***p*-LAcBDI** under a mild basic condition (*cat.* Piperidine, CH_2Cl_2) successfully rendered ***p*-LHBDI** with a high yield of ∼91% (see Scheme 2). Detailed explanations of the synthesis and characterization of ***o*-LHBDI** and ***p*-LHBDI** are provided in SI. In the end, we used 2,4-dihydroxybenzaldehyde and imidazolinone derivatives as reactants in acetonitrile, and the successful Knoevenagel condensation gave **H2BDI** in high yield (∼90%, see Scheme 2, and SI for experimental details).

The crystal structure of ***o*-LHBDI** is shown in Figure 1, and the crystal data, bond lengths, and angles are listed in Table S2−S4. In the crystal, the phenol ring and the imidazole-4-one ring are exactly coplanar, as evidenced by a dihedral angle of zero degrees for both ∠N(2)−C(3)−C(4)-C(5) and ∠C(3)−C(4)−C(5)-C(6). This, in combination with a 2.556(3) Å bond distance for O(2)−N(2) and a 164(4)° angle for ∠N(2)•••H−O(2), strongly supports the existence of an intramolecular hydrogen bond under a seven-membered ring configuration. Consistent with this observation, the ^{1}H NMR

Scheme 1. Synthesis of *o*-LHBDI

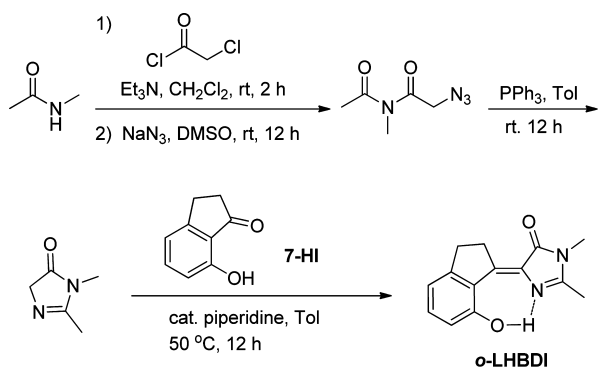

Scheme 2. Synthesis of *p*-LHBDI and H2BDI

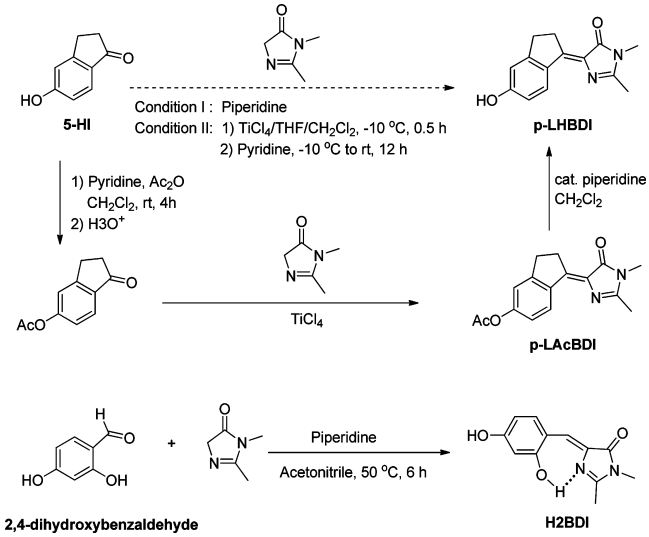

dx.doi.org/10.1021/ja5062856 | J. Am. Chem. Soc. 2014, 136, 11805−11812

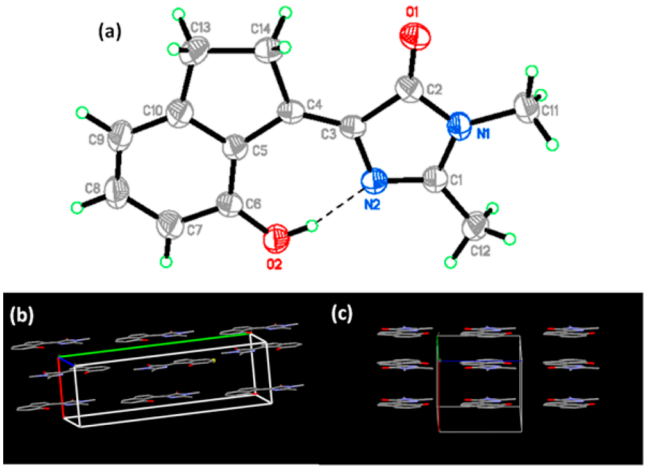

Figure 1. (a) The X-ray crystal structure for the ***o*-LHBDI** with thermal ellipsoids drawn at 50% probability level. (b) and (c) are packing diagrams of ***o*-LHBDI** viewed along the short and long axes, respectively.

spectrum reveals a significantly downfield shifted signal at 14.61 ppm for the hydroxyl proton (in $CDCl_3$, see Figure S8), confirming the formation of a strong hydrogen bond.

2.2. Photophysics of *o*-LHBDI. Figure 2 and Table 1 show the absorption and emission spectra of ***o*-LHBDI** in various

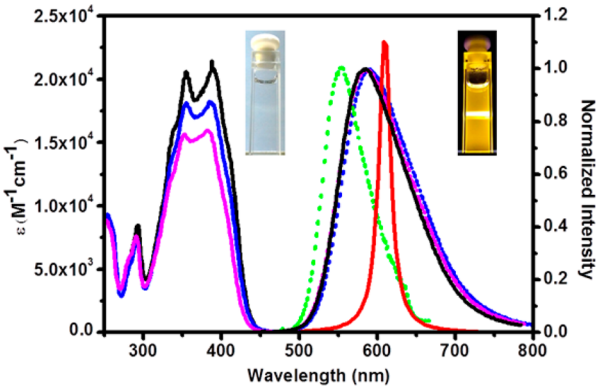

Figure 2. Steady-state absorption spectra (solid lines) and emission spectra (dotted lines) for ***o*-LHBDI** in toluene (black), CH_2Cl_2 (blue), acetonitrile (pink), and solid film (green). Also shown is the amplified spontaneous emission (ASE) in toluene. Inset: Photographs of the sample and its emission and ASE (the appearance of the intense stripe in the middle pumped by a line-shape 355 nm laser via a cylindrical lens).

solvents, in which the lowest-lying absorption band is located at 382−389 nm. The steady-state emission reveals a nearly solvent-polarity independent band maximized at 585−586 nm, for which the anomalously large Stokes shift of ∼9,000 cm^{-1} (absorption peak-to-emission peak) unambiguously leads us to assign a tautomer emission resulting from ESIPT. The tautomer emission profile is only slightly dependent on the solvent polarity, supporting the delocalized $\pi\pi^*$ transition character (see Table S5); i.e., with the elongation of π-conjugation upon forming the proton-transfer tautomer, the local charge transfer character is too small to induce the solvent polarity effect. The perfectly planar, seven-membered ring hydrogen-bonding configuration of ***o*-LHBDI** implies that ESIPT requires much less structural reorganization than the

Table 1. Photophysical Data for *o*-LHBDI, *p*-LHBDI, and H2BDI in different solvents and pH (in water) at room temperature

	λ_{abs}/nm (ε/$M^{-1}cm^{-1}$)	λ_{em}/nm	Φ_{em}	τ_{obs} [a]
	***o*-LHBDI**			
toluene	389 (20,700)	585	0.18	2.27 ns
CH_2Cl_2	387 (18,200)	586	0.10	1.51 ns
CH_3CN	382 (16,000)	585	0.09	1.50 ns
	***p*-LHBDI**			
EtOH	377 ([b])	434	1.2×10^{-4}	3.2 ps
H_2O (pH 10)	427 (32,500)	500	5.1×10^{-4}	5.8 ps
	H2BDI			
CH_2Cl_2	390 ([b])	574	1.1×10^{-3}	10.2 ps
H_2O (pH 8.5)	480 (57,700)	524	2.3×10^{-3}	18.5 ps
solid (or solid film)		555	0.50	5.60 ns

[a]Observed population decay time constant. [b]Solubility is too low for molar absorptivity measurements.

unlocked ***o*-HBDI**, or even none. This is clearly evidenced by the early relaxation dynamics measured by femtosecond fluorescence up-conversion technique (Figure 3). Monitoring

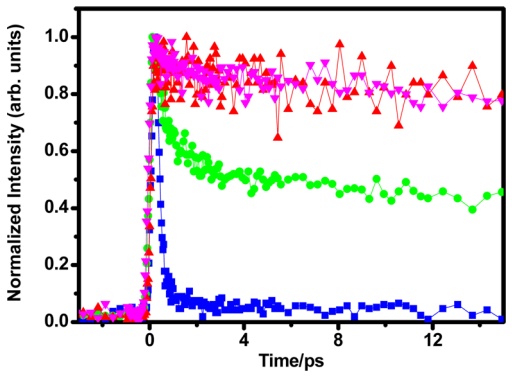

Figure 3. Time-resolved early relaxation dynamics of the upconverted fluorescence of the ***o*-LHBDI** in CH_2Cl_2 excited at 400 nm and monitored at 480 nm (blue), 550 nm (green), and 650 nm (red), and deuterated ***o*-LHBDI** in CD_2Cl_2 at 600 nm (pink line).

of the emission at 480 nm, which is attributed to the Franck−Condon normal emission region and is not observable in the steady-state measurement (see Figure 2), revealed that the decay time in CH_2Cl_2 exceeded the system response of 180 fs, confirming an ultrafast ESIPT process. Furthermore, upon monitoring at, e.g., 550 nm, the relaxation time traces could be convoluted by the sum of a system-response rise (<180 fs), a fast single exponential decay component of ∼1.1 ps, and a much longer decay component, which is nearly constant within the 15 ps acquisition time. Due to the highly exergonic ESIPT for ***o*-LHBDI**, the reaction free energy of which is calculated to be ∼ −6.4 kcal/mol (see Figure S1), the fast decay 1.1 ps component is assigned to be the rate of vibrational relaxation for the initially prepared, vibronically hot tautomer. In a longer wavelength region of, e.g., 650 nm, the vibrational relaxation decay component is expected to overlap with the rise of the emitting state, which has reached the thermal equilibrium, resulting in cancellation between rise and decay components. This delineation is consistent with the resolved time trace of the 650 nm emission (Figure 3), in which an ultrafast rise component appears, followed by a very long population decay

dx.doi.org/10.1021/ja5062856 | J. Am. Chem. Soc. 2014, 136, 11805−11812

component, which is virtually constant within the acquisition time window of 15 ps.

Upon deuteration (−OH to −OD), the time-dependent emission of O−D ***o*-LHBDI** in CD_2Cl_2 reveals similar results to its O−H counterpart in its early relaxation dynamics, consisting of the system response limited rise, a vibrational relaxation of a few ps decay that is wavelength dependent, and a much longer population decay component (see Figure 3 for the emission monitored at 600 nm). The results confirm that the ESIPT dynamics are insensitive to the H/D kinetic isotope effect, pointing to an essentially barrierless and perhaps coherent type of ESIPT along the reaction potential energy surface.[13]

Although the ESIPT phenomenon of ***o*-LHBDI** is similar to that of its unlocked counterpart ***o*-HBDI**, the remarkable difference lies in the much longer population decay time and hence the dramatic improvement of the emission quantum yield. The population decay of ***o*-LHBDI** was further resolved by a ps-ns time-correlated single photon counting technique. The lifetimes (quantum yields) were measured to be 2.27 ns (0.18), 1.51 ns (0.10), and 1.50 ns (0.09) in toluene, CH_2Cl_2, and CH_3CN, respectively. Comparing the weak tautomer emission of ***o*-HBDI** and its numerous unlocked derivatives in solution,[16,17] the ***o*-LHBDI** tautomer emission quantum yield of 0.18 in toluene is about 55 times higher than that of ***o*-HBDI** in the same solvent[18,26−28] and is believed to be a high emission yield among molecules bearing core benzylidene-imidazolinone moieties. This is also reflected by its 2.27 ns population lifetime, which is ∼60 times as long as the 38 ps of ***o*-HBDI**.

The intense, large Stokes shifted tautomer emission makes feasible the generation of the amplified spontaneous emission (ASE), the prerequisite for lasing action. For ***o*-LHBDI**, the ultrafast ESIPT and hence the instantaneous population at the tautomer emitting S_1 state, together with the lack of ground-state trapping, i.e., the non-existence of the ground-state tautomer local minimum according to the computational approach (see Figure S1), leads to a facile four-level electronic states to achieve population inversion and hence ASE. With an appropriate experimental setup (see Experimental Section), upon 355 nm laser excitation, ASE was readily observed (see Figure 2), with a gain coefficient calculated to be 7.1 at the peak wavelength of 598 nm. This gain coefficient is slightly lower than those of regular laser dyes.[19−21] However, since the emission quantum yield (0.18) is relatively lower than that (≫0.3) of the regular laser dyes, the results manifest the advantage of null loss of emission from the ground-state reabsorption due to the ∼9,000 cm^{-1} Stokes shifted emission (vide infra). This is also evidenced by the nearly matching peak wavelength between ASE and spontaneous emission, which is in sharp contrast to the much red-shifted ASE for laser dyes due to the reabsorption and the population inversion being achieved between S_1 (v = 0) and the vibrational hot state of S_0. Note that the ASE peak wavelength is slightly red-shifted (ca. 10−13 nm) from the maxima of spontaneous emission, mainly due to the λ^4 dependence of the ASE gain.[29]

In solid or solid film prepared by CVD, ***o*-LHBDI** exhibits a very intense tautomer 555 nm emission (quantum yield = 50%). However, we also noticed that the emission peak is blue-shifted by as large as 30 nm relative to that in solution (585 nm, see Figure 2). More importantly, as shown in Figure 2, the solid-state emission possesses a full width at half-maximum (fwhm) of ∼70 nm (2,180 cm^{-1}), which is much narrower than the fwhm of ∼110 nm (3,048 cm^{-1}) in solution. The fwhm of >3,000 cm^{-1} is also typical for all other *ortho*-GFP chromophores reported in both solid and solution.[16,17] The significant blue-shift and spectral narrowing in solid led us to consider the existence of a unique crystal packing for ***o*-LHBDI**. This unique packing may allow ***o*-LHBDI** to grow in a single crystal that also exhibits intense 555 nm tautomer emission. As shown in Figure 1b, in addition to the full planar structure, the unit cell shows a parallel head-to-tail packing, in which the phenol moiety in one layer interacts with the imidazole-4-one moiety in the other layer with a center-to-center distance of ∼3.4 Å, i.e., a configuration keen on an H-type of aggregation, and the layer angle θ = 65° (see Figures 1 and S2). Evidently, the H-type aggregation in ***o*-LHBDI** crystal explains the blue-shifted tautomer emission,[30−32] and the spectral narrowing plausibly results from rigid and tight H-packing. In contrast, the two layers of the unlocked ***o*-HBDI** in single crystal are staggered with a T-shape (see Figure S2), for which the $\pi-\pi$ interaction is negligible, rationalizing its similar emission spectral feature in both solid and solution.[12,13] Exploiting this unique property, ***o*-LHBDI** was thus applied as a narrow monochromatic lighting material in an OLED, as will be elaborated in a later section.

2.3. Photophysics of *p*-LHBDI and H2BDI. The locked form of the naturally occurring ***p*-HBDI**, i.e., ***p*-LHBDI** exhibits the lowest-lying absorption band, maximized at 377 nm in EtOH (Figure 4a). Unlike the non-emissive nature of the ***p*-HBDI**, ***p*-LHBDI** shows a weak emission band peaked at 434 nm. The emission spectral feature reveals a mirror image with respect to the absorption, and the emission quantum yield is measured to be 1.2 × 10^{-4} in ethanol. The solubility of ***p*-LHBDI** is sparse in neutral water but becomes soluble at pH >

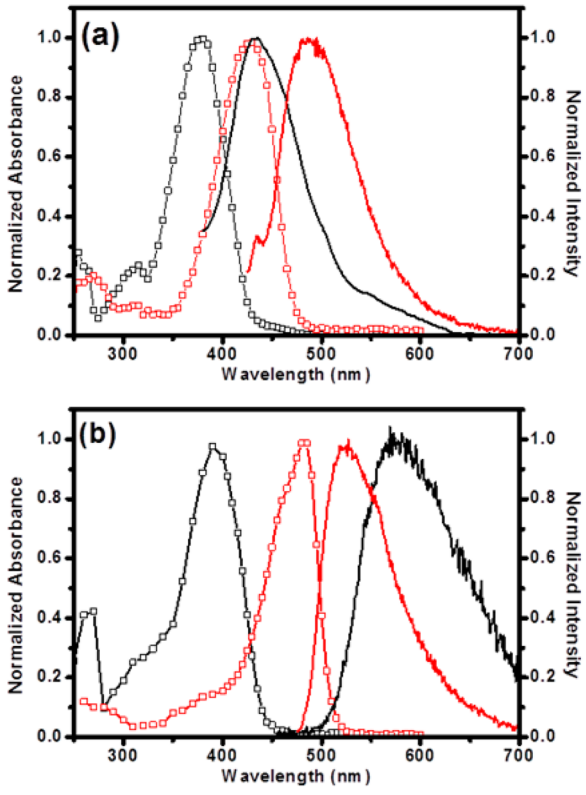

Figure 4. Steady-state absorption (□) and emission (solid line) spectra for (a) ***p*-LHBDI** in ethanol (black, λ_{ex}: 370 nm) and in water (pH 10, red, λ_{ex}: 400 nm) and (b) **H2BDI** in CH_2Cl_2 (black, λ_{ex}: 390 nm) and in water (pH 8.5, red, λ_{ex}: 400 nm).

dx.doi.org/10.1021/ja5062856 | J. Am. Chem. Soc. 2014, 136, 11805−11812

9 (pK_a ~ 8.2 for ***p*-LHBDI**, see Figure S3), forming an anionic species that mimics the GFP core chromophore. As a result, the ***p*-LHBDI** anion exhibits absorption at 427 nm and emission at 500 nm in water at pH 10. The ***p*-LHBDI** anion emission is a landmark among the isolated GFP chromophores to exhibit prominent green emission in aqueous solution. The quantum yield was measured to be 5.1×10^{-4}. Note that the emission of ***p*-LHBDI** reveals a shoulder around 530 nm in ethanol (Figure 4a), which is assigned to the anion emission originating from the excited-state deprotonation. The excited-state deprotonation of ***p*-LHBDI** in ethanol is not the focus of this study and hence will not be pursued further.

H2BDI possesses both *ortho*- and *para*-hydroxyl groups, in which the *ortho*-OH forms an intramolecular hydrogen bond with the N(2) nitrogen. Thus, similar to ***o*-LHBDI** (or ***o*-HBDI**) ESIPT is expected to take place in aprotic solvent such as CH_2Cl_2, revealing a large Stokes shifted tautomer emission maximized at 574 nm with respect to the lowest-lying absorption peak at 390 nm (see Figure 4b). In water of pH > ~6.8, deprotonation takes place, forming an anion species, as evidenced by the decrease of 390 nm neutral species accompanied by an appearance of a new band maximized at ~480 nm. At pH > ~8.5, an additional absorption band maximum at ~390 nm appears, while the 574 nm emission gradually decreases. **H2BDI** possesses two proton donating sites; therefore, the 480 nm can reasonably be assigned to the dianion species. By the absorption titration experiment, the pK_a of ***p*-HBDI** and ***o*-HBDI** were measured to be 8.40 and 8.87, respectively (see Figures S4 and S5). The higher pK_a in ***o*-HBDI** (cf. ***p*-HBDI**) can be rationalized by its intramolecular hydrogen-bonding formation. Accordingly, it is reasonable to assign the first and second deprotonated species of **H2BDI** to origins in the *para*- and *ortho*-OH sites, respectively. After carefully convoluting the absorption pH titration spectra (see Figure S6), pK_a for first and second deprotonation were deduced to be 7.5 and 9.4 for **H2BDI**. Accordingly, in pH 8.5, the *para*-OH deprotonated **H2BDI** should be the dominant species, which reveals the anion emission maximized at 524 nm (Figure 4b) with a quantum yield of 2.3×10^{-3}.

In a previous report,[16] we proposed that the deactivation of ***o*-HBDI** in the excited state occurs mainly through a one-bond-flip mechanism, and for ***p*-HBDI**, it is via a hula-twist motion. Here, we strategically designed ***o*-LHBDI** and ***p*-LHBDI**, in which rotation along the C4−C5 bond (see Chart 1) is prohibited. If the C4−C5 one-bond-flip quenching mechanism is the major deactivation channel for ***o*-LHBDI**, we would expect the emission quantum yield and lifetime to be drastically increased, consistent with the experimental result of ~60-fold increase in the emission yield (cf. ***o*-HBDI**), supporting the proposed mechanism from the chemistry point of view. However, since the quantum yield of ***o*-LHBDI** is smaller than unity, it seems that neither the one-bond flip nor the hula-twist motion alone can explain the current results.[33] On the other hand, although the C4−C5 locked form ***p*-LHBDI** did show an increase in the emission to the observable level, the emission was still weak, indicating that in addition to the emission quenching associated with C4−C5 bond rotation C3−C4 rotation in the excited state also plays an important role, rendering indirect support for the deactivation pathway incorporating a cooperative or hula-twist type of motion. Lastly, the dual (*ortho*- and *para*-) hydroxyl compound **H2BDI** (see Chart 1), in which C3−C4−C5 rotation is partially locked by intramolecular hydrogen-bond bonding, further illustrates the structure-luminescence relationship. Upon deprotonation of the *para*-OH proton, forming an anion in water (pH ~ 8.5), the corresponding 524 nm anion emission has a quantum yield of 2.3×10^{-3}, supporting the boost of emission yield via the structural constraint associated with intramolecular hydrogen bond. Therefore, for the titled **HBDI** analogues, independent of *ortho*- or *para*-OH, the twisting motions associated with the C(3)−C(4)−C(5) bonds contribute to the excited-state deactivation, which can be suppressed by covalent cyclization, intramolecular hydrogen-bonding formation, or both. On this basis, we may reasonably predict a high emission yield of the anion form of **H2LHBDI** (see Chart 1), for which the structure is doubly locked by cyclization and hydrogen bond simultaneously. In light of this, much effort has been made to synthesize **H2LHBDI**, but unfortunately to no avail, due mainly to an unknown polymerization reaction.

2.4. Application in OLED. Realizing the highly emissive feature of the proton-transfer tautomer, we further attempted to use ***o*-LHBDI** to fabricate an OLED. The electrochemical behavior of ***o*-LHBDI** was investigated by cyclic voltammetry using ferrocene as the internal standard. The oxidation and reduction potentials were measured to be −5.43 and −2.58 eV (versus vacuum, see Figure S7), respectively. Accordingly, OLED was successfully fabricated in a configuration of ITO/PEDOT:PSS (30 nm)/TAPC (25 nm)/CBP: ***o*-LHBDI** 30 wt % (25 nm)/TPBI (50 nm)/LiF/Al. Here, we used 4,4′-bis(9-carbazolyl)-2,2′-biphenyl (CBP) as a host, since it possesses suitable energy levels (HOMO = −5.9 eV and LUMO = −2.6 eV) to confine the excitons within the guest emitter.[34] The conducting polymer polyethylene dioxythiophene:polystyrene-sulfonate (PEDOT:PSS) was used as the hole-injection layer. We used 1,1′-bis[4-[*N*,*N*-di(*p*-tolyl)amino]phenyl] cyclohexane (TAPC)[35] with a thickness of 25 nm as the hole-transport layer and 1,3,5-tris(*N*-phenylbenzimidizol-2-yl)benzene (TPBI)[36] as the electron-transport layer to block the holes and facilitate electron injection/transportation. LiF and Al served as the electron-injection layer and cathode, respectively. Figure 5 presents the *J*−*V*−*L* characteristics, device efficiencies, and EL spectra of the device. Consequently, a yellow EL spectrum (λ_{max} ~ 568 nm, see Figure 5, inset) for the ***o*-LHBDI** based OLED could be obtained with a narrow fwhm of ~70 nm. The spectrum corresponded well with the thin film PL spectrum shown in Figure 2, indicating the retention of the H-type-like aggregation structure.

The device showed a low turn-on voltage of 3 V and a maximum brightness (L_{max}) as high as 54,500 cd/m^2 at 14 V (2,380 mA/cm^2). CIE coordinates of (0.47, 0.51) and a maximum external quantum efficiency (η_{ext}) of 1.9%, which corresponded to a current efficiency (η_c) of 5.9 cd/A and a power efficiency (η_p) of 3.2 lm/W, were also achieved. The external electroluminescence (EL) quantum efficiency (η_{ext}) of an OLED is a key parameter and can be described by this equation: $\eta_{ext} = \eta_{int} \times \eta_{out} = (\gamma \times \eta_\gamma \times \Phi_{PL}) \times \eta_{out}$; where η_{int} is the internal EL quantum efficiency and η_{out} is the light-out-coupling efficiency. According to the equation, η_{int} is limited by the following three factors: (i) charge balance of injected holes and electrons (γ), (ii) efficiency of radiative exciton production (η_γ), and (iii) photoluminescence (PL) quantum yield of the emitter molecules (Φ_{PL}). The η_{int} for the traditional fluorescence-based OLEDs is limited to <25% even in the ideal case. The outcoupling efficiency (η_{out}) for conventional bottom-emitting devices is usually only about 20%. Therefore, the maximum value of η_{ext} in OLEDs using conventional

dx.doi.org/10.1021/ja5062856 | J. Am. Chem. Soc. 2014, 136, 11805−11812

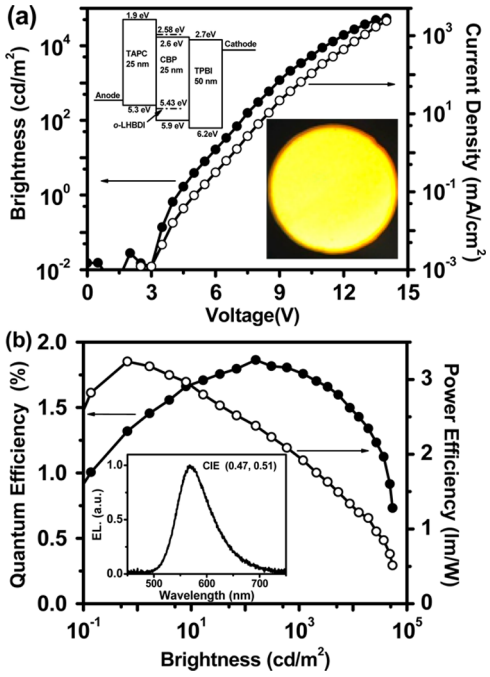

Figure 5. (a) Brightness (●) and current density (○) vs voltage characteristics of the ***o*-LHBDI** based OLED. Inset: Energy diagram of device. (b) External quantum (●) and power (○) efficiencies as a function of brightness. Inset: EL spectrum of the device.

fluorescence-based emitters is 5%. In our case, the ***o*-LHBDI** exhibits a Φ_{PL} of ca. 50% in the solid form or as a solid film prepared by CVD, so an η_{ext} of 1.9% for the device is satisfactory.

3. CONCLUSION

The high fluorescence quantum yield of the GFP core chromophore can be attributed to the protein cavity conformation, which can suppress non-radiative relaxation not only by restricting large-amplitude motions (rotation and bending about bonds) but also by reducing the degree of small-amplitude motions (vibration and stretching). Our aim is to prove that inhibiting the inherent rotational motion of the GFP core chromophores by either cyclization involving C(5)−C(6) single bond or forming the intramolecular hydrogen to restrict the C(3)−C(4)−C(5) motion will also lead to a suppression of radiationless deactivation and hence an increase in emission quantum yield. Various methodologies have thus been tested and reported in an aim to circumvent the synthesis hurdle. The designated compounds were successfully synthesized and showed dramatic improvement in their corresponding emission quantum yields

In aqueous solutions of pH > 7, the anion of ***p*-LHBDI** exhibits a prominent green emission at 500 nm with an emission quantum yield of 0.05%, which is an improvement over the lack of emission for ***p*-HBDI** anion and most isolated anion forms of GFP relevant chromophores.[37] In addition, partially restricting the C(3)−C(4)−C(5) via intramolecular hydrogen-bonding formation, as in the case of **H2BDI**, further increases the anion emission yield to 0.23%. As for ***o*-LHBDI**, ultrafast ESIPT takes place, resulting in an intense and large Stokes-shifted tautomer emission at ∼585 nm in solution. The emission quantum yield of 18% in toluene is high: ∼ 60 times as much as that of ***o*-HBDI**. The increase in the emission quantum yields for *ortho*-, *para*-**HBDI**, and **H2BDI** proves that the twisting motions along C(3)−C(4)−C(5) account for the radiationless deactivation. In comparison to ***p*-LHBDI**, the much higher emission quantum yield of ***o*-LHBDI** reveals that in addition to the inhibition of C(4)−C(5) motion via cyclization, the twisting along C(3)−C(4) is restricted, in part, by the intramolecular hydrogen bond, imposing a virtually double-locked configuration.

The advantageous four-electronic ESIPT levels, together with intense emission (Φ_{em} ∼ 0.18 in toluene), make possible the observation of ASE. Nevertheless, as for ***o*-LHBDI**, despite the double lock constraint, the single hydrogen-bonding strength (supposed to be <4 kcal/mol) is not high enough to restrict all motions. Certain small amplitude motions associated with the hydrogen bond may induce radiationless deactivation. Under a "frozen" condition such as in solid state, the emission yield of ***o*-LHBDI** can be as high as 50%, and fabrication of an ***o*-LHBDI** ESIPT-based OLED has been achieved. Given the advantage of the well-ordered H-like interaction in solid, the resulting narrow monochromatic light for ***o*-LHBDI** has a potential for large throughput in a display industry utilizing color-filter technology. In addition to their ubiquitous exploitation in bioimaging and biosensing,[5] we thus demonstrate that the GFP core chromophores, upon modification, may be geared to another avenue en route to optoelectronic applications.

4. EXPERIMENTAL SECTION

4.1. Synthesis and Characterization. All solvents were distilled from appropriate drying agents prior to use. Commercially available reagents were used without further purification unless otherwise stated. All reactions were monitored by TLC. Column chromatography was carried out using silica gel from Merck (230−400 mesh). ^{1}H and ^{13}C NMR spectra were recorded on a Varian Unity 400 spectrometer at 400 and 100 MHz, respectively. Chemical shifts (δ) are recorded in parts per million (ppm) and coupling constants (J) are reported in Hertz (Hz). Low- and high-resolution mass spectra were obtained using gas chromatograph−mass spectrometer (Finnigan MAT TSQ-46C GC/MS/MS/DS).

*4.1.1. Synthesis of (Z)-4-(7-hydroxy-2,3-dihydro-1H-inden-1-ylidene)-1,2-dimethyl-1H-imidazol-5(4H)-one (**o-LHBDI**).* A catalytic amount of piperidine (133 μL, 0.054 mmol) in a syringe was added to a solution of 7-hydroxy-1-indanone (40 mg, 0.27 mmol) and 1,2-dimethyl-1*H*-imidazol-5(4*H*)-one (33 mg, 0.30 mmol) in 35 mL of toluene. After stirring at room temperature for 12 h, the solvent was removed under reduced pressure. The crude product and impurities were separated by flash chromatography (EtOAc/hexanes 1:2) and recrystallized from EtOAc/hexanes to afford the ***o*-LHBDI** (41 mg, 63%) as a yellow solid. ^{1}H NMR (400 MHz, $CDCl_3$) δ 14.61 (br, 1H), 7.30−7.22 (m, 1H), 6.81 (dd, J = 7.2, 1.2 Hz, 1H), 6.76 (dd, J = 8.4, 1.2 Hz, 1H), 3.36 (t, J = 6.4 Hz, 2H), 3.20 (s, 3H), 3.1 (t, J = 6.4 Hz, 2H), 2.35 (s, 3H). ^{13}C NMR (100 MHz, $CDCl_3$) δ 167.00, 157.07, 154.65, 153.74, 152.99, 134.91, 126.77, 125.06, 115.83, 115.49, 30.69, 30.64, 26.48, 14.88. MS (EI, 70 eV): m/z (relative intensity) 242 (M^+, 100); HRMS calcd. for $C_{14}H_{14}N_2O_2$, 242.1055; found, 242.1051.

Deuteration of ***o*-LHBDI** was performed by dissolving ***o*-LHBDI** in methanol-d_4 followed by the evaporation of solvent. This procedure was repeated three times, which is sufficient to reduce the O−H ^{1}H NMR peak by ∼93%.

*4.1.2. Synthesis of (Z)-1-(1,2-dimethyl-5-oxo-1H-imidazol-4(5H)-ylidene)-2,3-dihydro-1H-inden-5-yl acetate (**p-LAcBDI**).* A solution of $TiCl_4$ (1.2 mL, 10.52 mmol) in CH_2Cl_2 (10 mL) was added into THF (45 mL) at −10 °C. To the solution, 1-oxo-2,3-dihydro-1*H*-inden-5-yl acetate (500 mg, 2.63 mmol) and 1,2-dimethyl-1*H*-imidazol-5(4*H*)-one (590 mg, 5.26 mmol) were subsequently added and allowed to stand at −10 °C for 40 min. Pyridine (0.85 mL, 10.52 mmol) was then added over a 30 min period. The reaction mixture was stirred at −10 °C for an additional 2 h and then allowed to stand

dx.doi.org/10.1021/ja5062856 | J. Am. Chem. Soc. 2014, 136, 11805−11812

overnight at room temperature. A saturated solution of NH_4Cl (40 mL) was added to the mixture and stirred for 10 min. The mixture was extracted with ethyl acetate (20 mL × 3), and the organic extracts were combined, dried over anhydrous $MgSO_4$, filtered, and concentrated. The residue was purified using column chromatography on silica gel (EtOAc/hexanes1:1) to yield the ***p*-LAcBDI** (340 mg, 45%) as a yellow solid. ^{1}H NMR (400 MHz, $CDCl_3$) δ 8.67 (d, J = 8.8 Hz, 1H), 7.08−7.07 (m, 1H), 7.01 (dd, J = 8.8, 2.0 Hz, 1H), 3.37 (t, J = 5.2 Hz, 2H), 3.18−3.12 (m, 5H), 2.89 (s, 3H), 2.32 (s, 3H). ^{13}C NMR (100 MHz, $CDCl_3$) δ 167.71, 169.19, 157.79, 152.91, 152.71, 148.99, 137.50, 132.25, 129.95, 120.72, 118.09, 30.78, 30.47, 26.32, 21.14, 15.14. MS (EI, 70 eV): m/z (relative intensity) 284 (M^+, 100); HRMS calcd. for $C_{16}H_{16}N_2O_3$, 284.1161; found, 284.1158.

*4.1.3. Synthesis of (Z)-4-(5-hydroxy-2,3-dihydro-1H-inden-1-ylidene)-1,2-dimethyl-1H-imidazol-5(4H)-one (**p-LHBDI**).* To a solution of ***p*-LAcBDI** (200 mg, 0.704 mmol) in CH_2Cl_2 was added a catalytic amount of piperidine (348 μL, 0.04 mmol). The reaction mixture was stirred at room temperature for 2 h, and the solvent was removed under reduced pressure. The crude product was recrystallized from CH_2Cl_2/MeOH to afford the ***p*-LHBDI** (155 mg, 91%) as a yellow solid. ^{1}H NMR (400 MHz, DMSO-d_6) δ 8.41 (d, J = 0.8 Hz, 1H), 6.74−6.71 (m, 2H), 3.14 (t, J = 5.6 Hz, 2H), 3.05 (s, 3H), 2.99 (t, J = 5.6 Hz, 2H), 2.25 (s, 3H). ^{13}C NMR (100 MHz, DMSO-d_6) δ 168.82, 160.66, 156.95, 153.82, 148.47, 130.74, 130.05, 129.79, 115.32, 112.26, 30.04, 25.95, 15.01. MS (EI, 70 eV): m/z (relative intensity) 242 (M^+, 100); HRMS calcd. for $C_{14}H_{14}N_2O_2$, 242.1055; found, 242.1053.

*4.1.4. Synthesis of (Z)-4-(2,4-dihydroxybenzylidene)-1,2-dimethyl-1H-imidazol-5(4H)-one (**H2BDI**).* A catalytic amount of piperidine (360 μL, 0.036 mmol) in a syringe was added to a solution of 2,4-dihydroxybenzaldehyde (100 mg, 0.73 mmol) and 1,2-dimethyl-1*H*-imidazol-5(4*H*)-one (89 mg, 0.8 mmol) in 35 mL of acetonitrile. After stirring at 50 °C for 6 h, the solvent was removed under reduced pressure. The crude product and impurities were separated by flash chromatography (1:2 EtOAc/hexanes +3% MeOH) and recrystallized from EtOAc/hexanes to afford the **H2BDI** (168 mg, 90%) as a yellow solid. ^{1}H NMR (400 MHz, DMSO-d_6) δ 12.52 (br, 1H), 10.20 (br. 1H), 7.99 (d, J = 8.4 Hz, 1H), 7.26 (s, 1H), 6.45 (dd, J = 8.4, 1.6 Hz, 1H), 6.41 (d, J = 1.6 Hz, 1H), 3.25 (s, 3H), 2.48 (s, 3H). ^{13}C NMR (100 MHz, DMSO-d_6) δ 168.26, 162.43, 159.85, 159.10, 136.34, 131.96, 124.73, 112.45, 108.28, 103.21, 26.35, 15.03 MS (EI, 70 eV): m/z (relative intensity) 232 (M^+, 100); HRMS calcd. for $C_{12}H_{12}N_2O_3$, 232.0848; found, 232.0845.

4.2. X-ray Structure Analysis. Single-crystal X-ray diffraction data were acquired on a Bruker SMART CCD diffractometer using λ (Mo-Kα) radiation (λ = 0.710 73 Å). The data collection was executed using the SMART program. Cell refinement and data reduction were carried out with the SAINT program. The structure was determined using the SHELXTL/PC program and refined using full-matrix least-squares. All non-hydrogen atoms were refined anisotropically, whereas hydrogen atoms were placed at calculated positions and included in the final stage of refinements with fixed parameters.

4.3. Steady-State and Time-Resolved Fluorescence Spectroscopy. Steady-state UV−vis absorption and emission spectra were recorded using a Hitachi (U-3310) spectrophotometer and an Edinburgh (FS920) fluorometer, respectively. The excitation light source of the fluorometer was corrected. In addition, the wavelength-dependent characteristics of the monochromator and photomultiplier were calibrated by recording the scattered light spectrum of the corrected excitation light from a diffused cell in the 220−700 nm range. All photophysical measurements in this study were performed at room temperature (298 K), and all solvents (spectroscopic grade, Merck Inc.) were used upon receiving without further purifications.

Nanosecond lifetime studies were performed with an Edinburgh FL 900 photon-counting system with a hydrogen- or nitrogen-filled lamp as the excitation source with 40 kHz repetition rate. Pico-nanosecond time-resolved fluorescence measurement was performed using the Edinburgh OB 900-L time-correlated single photon counting system (TCSPC) and the second harmonic generation (450 nm) from a femtosecond oscillator (Tsunami, Spectra-Physics) as the excitation light source. Emission was collected at right angle with respect to the pump. After deconvolution from the system response function, a temporal resolution of ∼30 ps can be reliably obtained. A polarizer was placed in the emission path to set the emission polarization parallel, perpendicular, or at the magic angle (54.7°) with respect to that of the pump laser for anisotropy measurements.

The femtosecond fluorescence up-conversion (FOG100, CDP) was utilized to study ultrafast dynamics (e.g., solvent relaxation) of the titled compounds. The excitation light source was generated from the same femtosecond oscillator. The cross correlation (instrument response function) obtained from the Raman scattering signal showed a fwhm of ∼180 fs and therefore a temporal resolution of ∼130 fs after deconvolution could be obtained. The polarization of the excitation laser pulses was set parallel, vertical, or at the magic angle (54.7°) by a $\lambda/2$ waveplate with respect to the detection polarization direction for ultrafast anisotropic measurement or anisotropy-free fluorescence decay.

The measurement of amplified spontaneous emission (ASE) was done by using a third harmonic (355 nm) of Nd:YAG laser as a pumping source. The doughnut shape beam was reshaped and focused by a cylindrical lens into a line shape with ∼10 mm length and 1 mm width, which excited the sample cuvette containing the solution. The sample cuvette is aligned in a Brewster angle with respect to the incident beam. The ASE traveled ∼50 cm before passing a pinhole (∼2 mm in diameter) to eliminate any unwanted spontaneous emission. The ASE output after the pinhole was then focused onto the slit of the monochromator and detected by an intensified charge coupled detector with its gated window open in synchrony with the pumping pulse. The gain coefficient, $\alpha(\lambda)$, of ASE was calculated by the equation expressed as

$$\alpha(\lambda) = \frac{2}{L}\ln\left[\frac{I_L}{I_{L/2}} - 1\right]$$

where L is the cell length being illuminated, I_L and $I_{L/2}$ denote the ASE intensity measured from the entire cell length and the cell half-length.

4.4. OLED Device Fabrication. All chemicals were subjected to purification at least once by temperature-gradient sublimation before use in this study. In a general procedure, ITO-coated glass substrates were washed with detergent, deionized water, acetone, and then methanol. Polyethylene dioxythiophene:polystyrenesulfonate (PEDOT:PSS) was spin coated onto the ITO substrates under ambient atmosphere yielding a layer of 30 nm, which were baked at 130 °C for 30 min to remove residual water. Subsequently, organic layers were thermally evaporated on top of the hole-injection layer at a base pressure of 10^{-6} Torr at room temperature. Thicknesses were monitored using a crystal oscillator during deposition and were verified later with spectroscopic ellipsometry. The deposition rate of each organic material was ca. 1−2 Å/s. Subsequently, LiF was deposited at 0.1 Å/s and then capped with Al (ca. 5 Å/s) through shadow masking without breaking the vacuum. The current density−voltage−luminance (J−V−L) characteristics of the devices were measured simultaneously in a glovebox using a Keithley 6430 Source Meter and a Keithley 6487 Picoammeter equipped with a calibration Si-photodiode. EL spectra were measured using a photodiode array (Ocean Optics USB2000+).

■ ASSOCIATED CONTENT

Ⓢ Supporting Information

Additional crystallographic (including CIF) and spectroscopic data are provided. This material is available free of charge via the Internet at http://pubs.acs.org.

■ AUTHOR INFORMATION

Corresponding Authors

wenhung@mail.ntou.edu.tw
chop@ntu.edu.tw

Author Contributions

[¶]These authors contributed equally.

Notes

The authors declare no competing financial interest.

■ ACKNOWLEDGMENTS

P.-T. C. thanks the Ministry of Science and Technology, Taiwan for the financial support.

■ REFERENCES

(1) Van Oort, B.; Ter Veer, M. J. T.; Groot, M. L.; Van Stokkum, I. H. M. *Phys. Chem. Chem. Phys.* **2012**, *14*, 8852−8858.
(2) Rafiq, S.; Rajbongshi, B. K.; Nair, N. N.; Sen, P.; Ramanathan, G. *J. Phys. Chem. A* **2011**, *115*, 13733−13742.
(3) Doerr, A. *Nat. Methods* **2011**, *8*, 790−791.
(4) Paige, J. S.; Wu, K. Y.; Jaffrey, S. R. *Science* **2011**, *333*, 642−646.
(5) Clark, J.; Grznarova, P.; Stansell, E.; Diehl, W.; Lipov, J.; Spearman, P.; Ruml, T.; Hunter, E. *Plos One* **2013**, *8*, e83863.
(6) Saha, R.; Verma, P. K.; Rakshit, S.; Saha, S.; Mayor, S.; Pal, S. K. *Sci. Rep.* **2013**, *3*, 1580.
(7) Donner, J. S.; Thompson, S. A.; Kreuzer, M. P.; Baffou, G.; Quidant, R. *Nano Lett.* **2012**, *12*, 2107−2111.
(8) Cheng, P.-H.; Li, C.-L.; Her, L.-S.; Chang, Y.-F.; Chan, A. W. S.; Chen, C.-M.; Yang, S.-H. *Brain Struct. Funct.* **2013**, *218*, 283−294.
(9) Pan, Y.; Leifert, A.; Graf, M.; Schiefer, F.; Thoroe-Boveleth, S.; Broda, J.; Halloran, M. C.; Hollert, H.; Laaf, D.; Simon, U.; Jahnen-Dechent, W. *Small* **2013**, *9*, 863−869.
(10) Addison, K.; Heisler, I. A.; Conyard, J.; Dixon, T.; Page, P. C. B.; Meech, S. R. *Faraday Discuss.* **2013**, *163*, 277−296.
(11) Losfeld, M.-E.; Soncin, F.; Ng, B. G.; Singec, I.; Freeze, H. H. *FASEB* **2012**, *26*, 4210−4217.
(12) Stavrov, S. S.; Solntsev, K. M.; Tolbert, L. M.; Huppert, D. *J. Am. Chem. Soc.* **2006**, *128*, 1540−1546.
(13) Gepshtein, R.; Huppert, D.; Agmon, N. *J. Phys. Chem. B* **2006**, *110*, 4434−4442.
(14) Usman, A.; Mohammed, O. F.; Nibbering, E. T. J.; Dong, J.; Solntsev, K. M.; Tolbert, L. M. *J. Am. Chem. Soc.* **2005**, *127*, 11214−11215.
(15) Chen, K. Y.; Cheng, Y. M.; Lai, C. H.; Hsu, C. C.; Ho, M. L.; Lee, G. H.; Chou, P. T. *J. Am. Chem. Soc.* **2007**, *129*, 4534−4535.
(16) Hsieh, C. C.; Chou, P. T.; Shih, C. W.; Chuang, W. T.; Chung, M. W.; Lee, J.; Joo, T. *J. Am. Chem. Soc.* **2011**, *133*, 2932−2943.
(17) Chuang, W. T.; Hsieh, C. C.; Lai, C. H.; Lai, C. H.; Shih, C. W.; Chen, K. Y.; Hung, W. Y.; Hsu, Y. H.; Chou, P. T. *J. Org. Chem.* **2011**, *76*, 8189−8202.
(18) Zhao, J. Z.; Ji, S. M.; Chen, Y. H.; Guo, H. M.; Yang, P. *Phys. Chem. Chem. Phys.* **2012**, *14*, 8803−8817.
(19) Baldridge, A.; Solntsev, K. M.; Song, C.; Tanioka, T.; Kowalik, J.; Hardcastle, K.; Tolbert, L. M. *Chem. Commun.* **2010**, *46*, 5686−5688.
(20) Wu, L. X.; Burgess, K. *J. Am. Chem. Soc.* **2008**, *130*, 4089−4096.
(21) Baranov, M. S.; Lukyanov, K. A.; Borissova, A. O.; Shamir, J.; Kosenkov, D.; Slipchenko, L. V.; Tolbert, L. M.; Yampolsky, I. V.; Solntsev, K. M. *J. Am. Chem. Soc.* **2012**, *134*, 6025−6032.
(22) Fang, X. X.; Wang, Y.; Wang, D.; Zhao, G. Y.; Zhang, W. W.; Ren, A. M.; Wang, H. Y.; Xu, J. W.; Gao, B. R.; Yang, W. *J. Phys. Chem. Lett.* **2014**, *5*, 92−98.
(23) Sharma, V.; Lansdell, T. A.; Jin, G. Y.; Tepe, J. J. *J. Med. Chem.* **2004**, *47*, 3700−3703.
(24) Sharma, V.; Tepe, J. J. *Bioorg. Med. Chem. Lett.* **2004**, *14*, 4319−4321.
(25) Papeo, G.; Poster, H.; Borghi, D.; Varasi, M. *Org. Lett.* **2005**, *7*, 5641−5644.
(26) Tang, K. C.; Chang, M. J.; Lin, T. Y.; Pan, H. A.; Fang, T. C.; Chen, K. Y.; Hung, W. Y.; Hsu, Y. H.; Chou, P. T. *J. Am. Chem. Soc.* **2011**, *133*, 17738−17745.
(27) Demchenko, A. P.; Tang, K. C.; Chou, P. T. *Chem. Soc. Rev.* **2013**, *42*, 1379−1408.
(28) Lin, T. Y.; Tang, K. C.; Yang, S. H.; Shen, J. Y.; Cheng, Y. M.; Pan, H. A.; Chi, Y.; Chou, P. T. *J. Phys. Chem. A* **2012**, *116*, 4438−4444.
(29) Chou, P.; Mcmorrow, D.; Aartsma, T. J.; Kasha, M. *J. Phys. Chem.* **1984**, *88*, 4596−4599.
(30) Varghese, S.; Park, S. K.; Casado, S.; Fischer, R. C.; Resel, R.; Milian-Medina, B.; Wannemacher, R.; Park, S. Y.; Gierschner, J. *J. Phys. Chem. Lett.* **2013**, *4*, 1597−1602.
(31) Rosch, U.; Yao, S.; Wortmann, R.; Wurthner, F. *Angew. Chem., Int. Ed.* **2006**, *45*, 7026−7030.
(32) Choi, S.; Bouffard, J.; Kim, Y. *Chem. Sci.* **2014**, *5*, 751−755.
(33) Liu, R. S. H.; Hammond, G. S. *Proc. Natl. Acad. Sci. U.S.A.* **2000**, *97*, 11153−11158.
(34) Baldo, M. A.; Lamansky, S.; Burrows, P. E.; Thompson, M. E.; Forrest, S. R. *Appl. Phys. Lett.* **1999**, *75*, 4−6.
(35) Tang, C. W.; Vanslyke, S. A. *Appl. Phys. Lett.* **1987**, *51*, 913−915.
(36) Yeh, S. J.; Wu, M. F.; Chen, C. T.; Song, Y. H.; Chi, Y.; Ho, M. H.; Hsu, S. F.; Chen, C. H. *Adv. Mater.* **2005**, *17*, 285−289.
(37) Yang, J.-S.; Huang, G.-J.; Liu, Y.-H.; Peng, S.-M. *Chem. Commun.* **2008**, 1344−1346.